



Article

# SnO<sub>2</sub>/TiO<sub>2</sub> Thin Film n-n Heterostructures of Improved Sensitivity to NO<sub>2</sub>

Piotr Nowak <sup>1,\*</sup>, Wojciech Maziarz <sup>1</sup>, Artur Rydosz <sup>1</sup>, Kazimierz Kowalski <sup>2</sup>,  
Magdalena Ziabka <sup>3</sup> and Katarzyna Zakrzewska <sup>1</sup>

<sup>1</sup> Faculty of Computer Science, Electronics and Telecommunications, AGH University of Science and Technology, Al. Mickiewicza 30, 30-059 Kraków, Poland; maziarz@agh.edu.pl (W.M.); rydosz@agh.edu.pl (A.R.); zak@agh.edu.pl (K.Z.)

<sup>2</sup> Faculty of Metals Engineering and Industrial Computer Science, AGH University of Science and Technology, Al. Mickiewicza 30, 30-059 Kraków, Poland; kazimierz.kowalski@agh.edu.pl

<sup>3</sup> Faculty of Materials Science and Ceramics, AGH University of Science and Technology, Al. Mickiewicza 30, 30-059 Kraków, Poland; ziabka@agh.edu.pl

\* Correspondence: piotr.nowak@agh.edu.pl

Received: 30 September 2020; Accepted: 25 November 2020; Published: 29 November 2020



**Abstract:** Thin-film n-n nanoheterostructures of SnO<sub>2</sub>/TiO<sub>2</sub>, highly sensitive to NO<sub>2</sub>, were obtained in a two-step process: (i) magnetron sputtering, MS followed by (ii) Langmuir-Blodgett, L–B, technique. Thick (200 nm) SnO<sub>2</sub> base layers were deposited by MS and subsequently overcoated with a thin and discontinuous TiO<sub>2</sub> film by means of L–B. Rutile nanopowder spread over the ethanol/chloroform/water formed a suspension, which was used as a source in L–B method. The morphology, crystallographic and electronic properties of the prepared sensors were studied by scanning electron microscopy, SEM, X-ray diffraction, XRD in glancing incidence geometry, GID, X-ray photoemission spectroscopy, XPS, and uv-vis-nir spectrophotometry, respectively. It was found that amorphous SnO<sub>2</sub> films responded to relatively low concentrations of NO<sub>2</sub> of about 200 ppb. A change of more than two orders of magnitude in the electrical resistivity upon exposure to NO<sub>2</sub> was further enhanced in SnO<sub>2</sub>/TiO<sub>2</sub> n-n nanoheterostructures. The best sensor responses R<sub>NO<sub>2</sub></sub>/R<sub>0</sub> were obtained at the lowest operating temperatures of about 120 °C, which is typical for nanomaterials. Response (recovery) times to 400 ppb NO<sub>2</sub> were determined as a function of the operating temperature and indicated a significant decrease from 62 (42) s at 123 °C to 12 (19) s at 385 °C. A much smaller sensitivity to H<sub>2</sub> was observed, which might be advantageous for selective detection of nitrogen oxides. The influence of humidity on the NO<sub>2</sub> response was demonstrated to be significantly below 150 °C and systematically decreased upon increase in the operating temperature up to 400 °C.

**Keywords:** gas sensors; SnO<sub>2</sub>; TiO<sub>2</sub>; thin films; Langmuir-Blodgett technique

## 1. Introduction

Nitrogen dioxide (NO<sub>2</sub>) is a highly reactive, hazardous gas and a prominent air pollutant. Despite the fact that only very high concentrations of NO<sub>2</sub> cause immediate effects: mild irritation of the nose and throat (10–20 ppm), swelling leading to pneumonia or bronchitis (25–50 ppm), and death due to suffocation (above 100 ppm) [1], a prolonged exposure to low amounts of NO<sub>2</sub> (even of hundreds ppb) may cause breathing problems, including airway inflammation of healthy people and respiratory inefficiency for those with asthma. The threshold limit value (TLV) was set to 3 ppm as time-weighted average (TWA), and 5 ppm as short-term exposure limit (STEL) [2]. Low-threshold, highly sensitive and selective detection of NO<sub>2</sub> has recently appeared as a particularly important issue due to an increased global conscience of its detrimental influence on the environment [3,4]. Quite drastic measures taken in

the case of indoor monitoring of NO<sub>2</sub> in car interiors [5,6] related to the application of catalysts mounted in the automotive exhaust systems has driven the research towards new concepts of accumulative-type sensors [7].

Metal oxide semiconductors, MOS, such as SnO<sub>2</sub> and TiO<sub>2</sub> have been most frequently used as CO and H<sub>2</sub> gas sensors of the resistive-type [8–15]. Applications of these n-type semiconductors to oxidizing gases are relatively scarce as the resulting high resistance is often beyond the measurement limit. Recently, it has been recognized that it is possible to construct efficient NO<sub>2</sub> sensors based on Al doped SnO<sub>2</sub> able to operate properly even under the humidity background [16].

A literature review of SnO<sub>2</sub>-based sensing materials for detection of NO<sub>2</sub> synthesized by various physical and chemical methods is given in Table 1. From the data included in this table, one can conclude that the efforts are mainly focused on near to room-operating temperature and low NO<sub>2</sub> threshold. Depending on the composition of the sensing material, even extremely high responses corresponding to the electrical resistance change up to 4 orders of magnitude were demonstrated [17].

**Table 1.** Survey of NO<sub>2</sub>-sensing materials based on SnO<sub>2</sub> prepared by various physical and chemical methods.

NO <sub>2</sub> -Sensing MOS	Synthesis Method	Operating Temperature	R <sub>NO2</sub> /R <sub>air</sub>	Concentration [ppm]	Reference, Year
SnO <sub>2</sub>	rf-sputtering	200 °C	18	0.1	[18], 1997
SnO <sub>2</sub>	sol-gel	150 °C	72	500	[19], 2007
ZnO–SnO <sub>2</sub>	reversed microemulsion	250 °C	34.5	500	[20], 2008
WO <sub>2</sub> –SnO <sub>2</sub>	sol precipitation	200 °C	186	200	[21], 2010
In <sub>2</sub> O <sub>3</sub> –SnO <sub>2</sub>	co-precipitation	200 °C	7.5	1000	[22], 2006
TiO <sub>2</sub> /SnO <sub>2</sub>	e-beam evaporation	90 °C	825	10	[23], 2013
SnO <sub>2</sub>	chemical spray deposition	350 °C	60	500	[24], 1999
SnO <sub>2</sub>	vapor phase deposition	300 °C	9	0.2	[11], 2005
SnO <sub>2</sub>	chemical vapor deposition	450 °C	0.93	10	[25], 1999
SnO <sub>2</sub> +Bi <sub>2</sub> O <sub>3</sub>	vapor-liquid-solid method	250 °C	56.9	2	[26], 2018
SnO <sub>2</sub> + graphene SnO <sub>2</sub> +MWCNT	sol–gel method	RT	~9.5 ~4.5	20	[27], 2016
Au/SnO <sub>2</sub> :NiO	sputtering	200 °C	~185	5	[28], 2019
SnO <sub>2</sub>	spray pyrolysis	150 °C	556	40	[29], 2017
SnO <sub>2</sub> /SnS <sub>2</sub>	high temperature oxidation	80 °C	5	8	[30], 2017
Pd/SnO <sub>2</sub> Pt/SnO <sub>2</sub>	co-precipitation	30 °C + 7mW uv	3400 1500	5	[31], 2017
SnO–SnO <sub>2</sub>	hydrothermal method	RT	2.5 4.5 15	0.2 1 100	[32], 2018
SnO <sub>2</sub> -WO <sub>3</sub>	thermal decomposition	150 °C	12800	5	[17], 2018
SnO <sub>2</sub> -graphene	hydrothermal method	75 °C	225	0.35	[33], 2019
ZnO+SnO <sub>2</sub>	electrospinning	200 °C	258	100	[34], 2019
SnO <sub>2</sub> @SnS <sub>2</sub>	hydrothermal method	RT, blue light	5.2 57.3	0.2 5	[35], 2020
SnO <sub>2</sub> /ZnO	sputtering	100 °C	67	100	[36], 2020

RT—room temperature, uv—ultraviolet irradiation, MWCNT—multiwall carbon nanotubes; NT—nanotubes.

All these efforts indicate that the development of a stable and selective NO<sub>2</sub> gas sensor being capable of fast and accurate detection of extremely low NO<sub>2</sub> concentrations at near to room temperature is still of prime importance for environmental monitoring, public health and automotive applications.

Recently, a dramatically increased number of publications dealing with p-n and n-n heterostructures as a promising solution to gas sensitivity improvement has been observed [32,37–46]. In particular, TiO<sub>2</sub>-SnO<sub>2</sub> n-n heterostructures have been proposed as gas sensitive materials [38,39,45,46].

In 2010, Zeng et al. [39] explained the mechanism responsible for an improved sensitivity of n-n heterostructures. Results from independent experiments showed that the conduction (CB) and valence (VB) band edges of TiO<sub>2</sub> are above those corresponding to SnO<sub>2</sub>. Therefore, when physical connection is made between TiO<sub>2</sub> and SnO<sub>2</sub> grains, a contact potential difference is established which is responsible for an electron transfer from CB of TiO<sub>2</sub> to CB of SnO<sub>2</sub>. Then, the oxygen pre-adsorption at the surface of SnO<sub>2</sub> grains is enhanced due to electronic charge injection. Increased concentration of adsorption sites for oxygen is treated as a decisive factor for the observed improvement of the sensing behavior of SnO<sub>2</sub> with a small addition of TiO<sub>2</sub> [38,47].

To date, our research performed on TiO<sub>2</sub>-SnO<sub>2</sub> was related to the gas sensors based on solid-solutions and nanocomposites being a simple mixture of two constituents [38,46–48]. Thin films in a form of bi-layers have been studied with much smaller success [45] as the interfaces are usually flat, resulting in much lower surface-to-volume ratio. In order to benefit from both a planar geometry with well defined interfaces between layers and an increased surface-to-volume ratio, a combination of two methods—magnetron sputtering MS and the Langmuir-Blodgett technique—has been proposed in the present work. This innovative approach is expected to yield enhanced responses, particularly to oxidizing gases.

Recently, numerous attempts to use the Langmuir-Blodgett (L-B) technique to grow metal oxide thin films have been reported [49–54]. In contrast to Physical Vapour Deposition methods, PVD, [55–59], Langmuir-Blodgett is a non-destructive technique which does not change the structure of the substrate. However, it can affect its electrical properties. Moreover, the L-B deposition is carried out at room temperature and at a normal pressure.

Here, a non-destructive modification of SnO<sub>2</sub> layer (obtained via magnetron sputtering) by a thin film of TiO<sub>2</sub> deposited using L-B method is proposed for the construction of an efficient NO<sub>2</sub> sensor. To the best of our knowledge, this is the first report of application of such combination of methods in the development of SnO<sub>2</sub>/TiO<sub>2</sub> thin film n-n heterostructures for NO<sub>2</sub> detection at low concentration and temperature.

## 2. Materials and Methods

### 2.1. Sample Preparation

#### 2.1.1. SnO<sub>2</sub> Thin Films

Thin films of SnO<sub>2</sub> were deposited by magnetron sputtering from a metallic Sn target onto corundum CC2.S type supports (BVT Technologies, Czech Republic) dedicated to sensor measurements, silicon and amorphous silica a-SiO<sub>2</sub> substrates to study their morphological, structural and electronic properties. Reactive sputtering was performed at 50 W, in Ar + 20% O<sub>2</sub> atmosphere, with base and working pressures of  $1.0 \times 10^{-5}$  mbar and  $2.0 \times 10^{-2}$  mbar, respectively. Two types of SnO<sub>2</sub> samples—a-SnO<sub>2</sub> and c-SnO<sub>2</sub>—were prepared at a substrate temperature of 180 °C during 30 min of sputtering and at 200 °C during 120 min, respectively.

#### 2.1.2. TiO<sub>2</sub> Thin Films

TiO<sub>2</sub> thin films were deposited by the L-B method on previously grown a-SnO<sub>2</sub> thin films to form SnO<sub>2</sub>/TiO<sub>2</sub> n-n nanoheterostructures. Moreover, TiO<sub>2</sub> single layers were obtained on silicon and amorphous silica substrates for XRD, XPS, SEM and optical characterisation.

Langmuir trough and the idea of L–B technique are demonstrated in Figure 1. The experimental set-up consisted of KSV NIMA bath with 270 cm<sup>2</sup> total area by Biolin Scientific, placed on an anti-vibrational table (Figure 1a). Commercial TiO<sub>2</sub> rutile nanopowder (Sigma-Aldrich, St. Louis, MO, USA) with a specific surface area, SSA, of 140 m<sup>2</sup>/g was spread on the surface of subphase, i.e., the deionized water with a conductance less than 0.08 μS/cm and rapidly evaporating solvent composed of chloroform:ethanol with 4:1 *v/v* and a typical concentration of 0.5 mg/mL. After spreading, 10 min was allowed for the solvent to evaporate, leaving a loosely packed TiO<sub>2</sub> layer which was subsequently compressed to a certain surface tension by barriers moving with the speed of 2 mm/min. The surface tension was measured with an accuracy of ±0.1 mN/m using a Wilhelmy plate made of chromatographic paper (Whatman, Piscataway, NJ, USA).

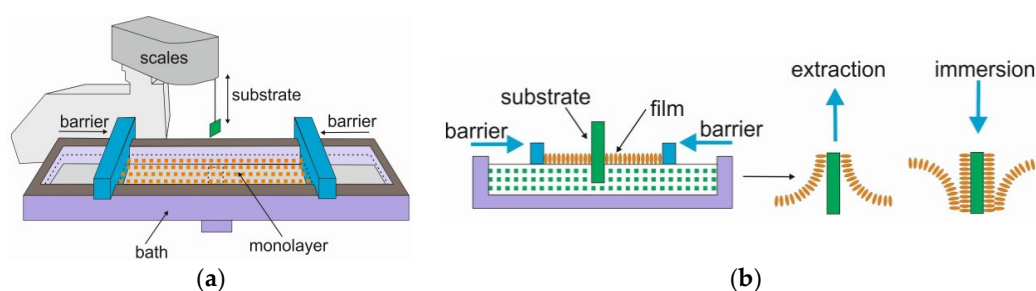


**Figure 1.** Langmuir–Blodgett deposition technique: (a) the setup, (b) the method idea.

Thin (60 nm) layers of TiO<sub>2</sub> were obtained by a transfer from the liquid–solid interface to the solid substrates by consecutive immersion and extraction, as shown in Figure 1b. All experiments were performed at room temperature.

Prior to this transfer, Langmuir isotherms of suspensions of TiO<sub>2</sub> rutile nanopowders spread on the surface of water in the Langmuir trough were recorded. The surface tension ( $\Pi$ ) as a function of total area between barriers ( $A$ ) for different volumes ( $V$ ) of spread TiO<sub>2</sub> suspension (100–1000 μL) is presented in Figure 2.

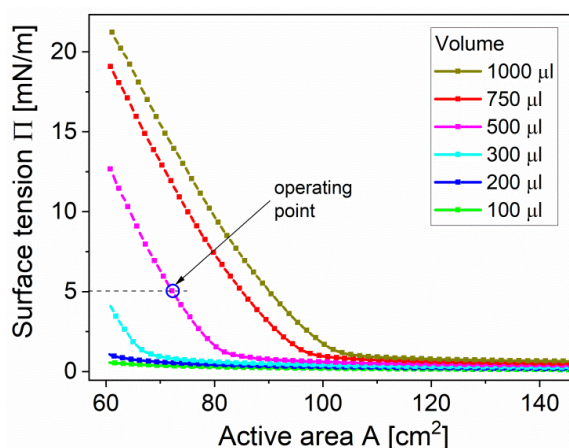


**Figure 2.** The surface tension vs. active inter-barrier area ( $\Pi$ - $A$  Langmuir isotherms) during deposition of TiO<sub>2</sub> thin film by L–B.

The isotherms reveal negligible changes of  $\Pi$  at large  $A$  until the film is compressed at about 110 cm<sup>2</sup>. Below  $A = 110$  cm<sup>2</sup> for volume  $V$  of spread TiO<sub>2</sub> suspension between 100 μL to 1000 μL the surface tension rises sharply until completely compressed in the trough at  $A = 60$  cm<sup>2</sup>. The point of rapid growth of value is strongly dependent on  $V$ . The highest  $\Pi$  equals to 22 mN/m as recorded at  $V = 1000$  μL. Even for high  $V$  values no collapse is observed, thus TiO<sub>2</sub> layers are stable.

Finally, the TiO<sub>2</sub> layers were deposited onto the bare substrates or SnO<sub>2</sub> covered ones at the surface tension  $\Pi = 5$  mN/m and spread volume  $V = 500$  μL.

## 2.2. Characterization Methods

The properties of the prepared thin films were investigated with the use of X-ray diffraction, XRD, scanning electron microscopy, SEM, X-ray photoelectron spectroscopy, XPS, and optical methods.

X-ray diffraction, XRD at grazing incidence GID allowed us to determine the crystal structure of the deposited films. Philips X'Pert Pro diffractometer with CuK $\alpha$  X-ray radiation with wavelength  $\lambda = 0.154056$  nm, at the incidence angle  $\omega = 3^\circ$ , was used. The crystallite size,  $D$ , was calculated from the Debye–Scherrer's formula given by

$$D = \frac{k\lambda}{\beta \cos \theta} \quad (1)$$

where  $k = 0.9$ ,  $\beta$  is the full width at half maximum (FWHM) of a diffraction peak and  $\theta$  is half of the angle at which a given diffraction peak occurs.

The morphology of SnO<sub>2</sub> and TiO<sub>2</sub> thin films grown on Si substrates was studied with a NOVA NANO SEM 200 (FEI) Scanning Electron Microscope SEM. The FEI Helios NanoLab 600i Scanning Electron Microscope was applied for the studies of growth of TiO<sub>2</sub> films on SnO<sub>2</sub> supports. A chemical analysis of elements was performed by means of Energy Dispersive Spectroscopy, EDS with the latter microscope.

X-ray Photoelectron Spectroscopy (XPS) was employed to assess the surface properties of deposited films. Experiments were performed with the VSW (Vacuum Systems Workshop Ltd., Crowborough, England) instrument working at K $\alpha$  Mg (1253.6 eV) X-ray radiation and equipped with a concentric hemispherical electron analyser, the details of which are given in [37]. For the calibration of the binding energy BE scale, it was assumed that the position of C 1s line of the adventitious carbon, corresponding to the C–H bond, was equal to 284.6 eV.

Optical spectra of the transmittance  $T$  and reflectance  $R$  coefficients over a wide wavelength range (220–2200 nm) corresponding to uv/vis/nir regions were taken with the help of Perkin Elmer Lambda 19 double beam spectrophotometer.

The sensors' responses were measured in a custom-made setup similar to that described elsewhere [60]. The measurements were performed on films deposited onto the final sensors' platforms, containing double IDT electrodes made of Au and Pt alloy, presented in Figure 3. Due to the double set of electrodes, it was possible to carry out simultaneous studies in both channels and compare the results of SnO<sub>2</sub>/TiO<sub>2</sub> with those of SnO<sub>2</sub> under the same conditions.

The sensors were installed in a gas chamber with volume  $\approx 30$  cm<sup>3</sup> on a heated workholder. The sensor temperature was determined with a Pt100 thermometer and Agilent 34970A digital multimeter. As the sensor resistance changed over few orders of magnitude, Keithley 6517 electrometer, which sourced a constant voltage  $U$  in the range of 1–10 V, was used for the measurement of sensor responses. When the current drawn by the sensor was measured, the sensor resistance was calculated. The samples were collected every 2 s with the use of LabVIEW application working on a PC computer. It controlled the system devices over IEEE 488 (GPIB) bus with the use of SCPI language. The desired gas atmosphere was prepared in a gas system comprised of bottles with synthetic air, NO<sub>2</sub>, H<sub>2</sub>, bubbler for humidifying purposes, and MKS Instruments mass flowmeters controlled with a custom-made mass flow and humidity controller. The sensors were exposed to hydrogen (H<sub>2</sub>, 1000 ppm in a bottle) and nitrogen dioxide (NO<sub>2</sub>, 100 ppm in a bottle), supplied by Air Products, Poland. The requested gas concentration was achieved by controlling the ratio of gas to air flow rate, while the humidity was set up by varying the ratio of dry to humidified air. A total gas flow of 500 cm<sup>3</sup>/min was kept constant during the whole measurement cycle. Prior to performing measurements, the sensor response was stabilized in a synthetic air under pre-set conditions (constant humidity, elevated temperature and chosen gas flow rate), following standard conditioning procedure. Then, the sensor response was measured using two scenarios. In the first one (CC-constant concentration), the sensor was exposed to a series of on/off NO<sub>2</sub> pulses of the same concentration, with the temperature rising in well defined



steps, as shown in Figure 4a. In the second scenario (CT-constant temperature), a series of on/off  $\text{NO}_2$  pulses of increasing concentrations was applied, while the temperature was kept constant (Figure 4b). From the measured sensor responses, one could calculate the basic sensor parameters: response,  $S$ , response time,  $t_{res}$ , and recovery time,  $t_{rec}$ . The sensor responses,  $S$ , were defined differently for reducing ( $\text{H}_2$ ) and oxidizing ( $\text{NO}_2$ ) gases. In order to obtain  $S$  higher than 1,  $S_{\text{H}_2} = R_0/R_{\text{H}_2}$  was taken as the electrical resistance in air  $R_0$  divided by that in hydrogen  $R_{\text{H}_2}$ , while the inverse ratio was used for  $\text{NO}_2$ , i.e.,  $S_{\text{NO}_2} = R_{\text{NO}_2}/R_0$ .

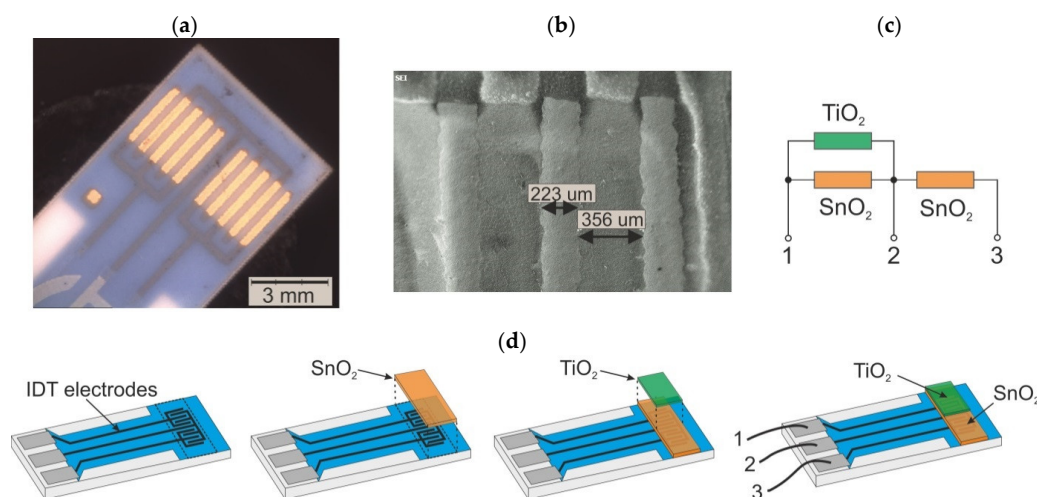


**Figure 3.** Gas sensor used in experiment: (a) SEM photograph of substrate with interdigital Au electrodes and (b) electrodes in magnification, (c) simplified equivalent circuit of the sensor, and (d) successive steps of gas sensor preparation, with sputtered  $\text{SnO}_2$  layer and  $\text{TiO}_2$  thin film deposited by the L-B technique.

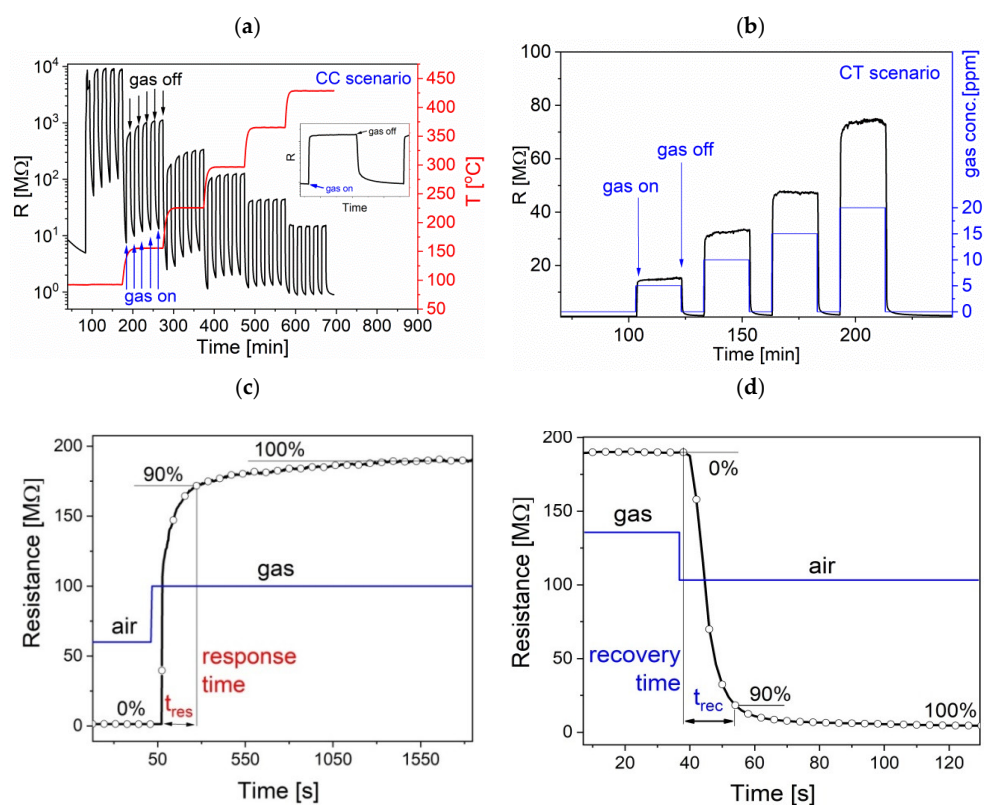


**Figure 4.** Gas sensor response measurements scheme according to (a) CC (constant concentration) and (b) CT (constant temperature) scenarios, and definitions of (c) response  $t_{res}$  and (d) recovery  $t_{rec}$  times.

The  $t_{\text{res}}$  and  $t_{\text{rec}}$  parameters were set up as a time required to change the electrical resistance by 90% from the base resistance measured in air (for  $t_{\text{res}}$ ) or gas (for  $t_{\text{rec}}$ ) to the stable signal value obtained after the gas or air were introduced, as shown in Figure 4c,d, respectively.

### 3. Results and Discussion

#### 3.1. Film Characterization

Glancing incidence GID X-ray diffraction XRD patterns of the most representative samples prepared in this work are shown in Figure 5. Single SnO<sub>2</sub> layers deposited by reactive magnetron sputtering on a-SiO<sub>2</sub> substrate belong to two classes: weakly crystallized almost amorphous a-SnO<sub>2</sub> and crystalline c-SnO<sub>2</sub>. This difference in the level of crystallization is due to the intentionally changed temperature and sputtering time. XRD pattern of SnO<sub>2</sub>/TiO<sub>2</sub> bi-layer, composed of a-SnO<sub>2</sub> thin film grown by magnetron sputtering with TiO<sub>2</sub> deposited on top of it by the Langmuir–Blodgett method, displays no additional peaks due to TiO<sub>2</sub> probably because of a small amount of this phase. Tetragonal tin dioxide cassiterite polymorphic form has been confirmed in c-SnO<sub>2</sub> samples by identification of the most prominent X-ray diffraction lines of crystallographic planes of (110), (101) and (211) with the reference JCPDS data of the card no. 77-0452 (ICSD #039178).

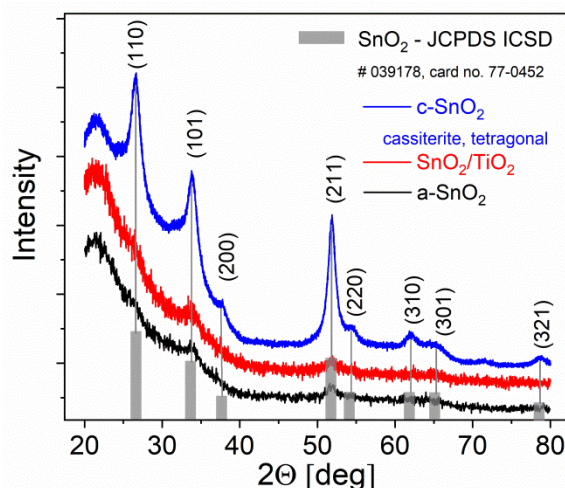


**Figure 5.** X-ray of diffraction, XRD, patterns of cassiterite, tetragonal SnO<sub>2</sub> phase, c-SnO<sub>2</sub>, amorphous a-SnO<sub>2</sub> and SnO<sub>2</sub>/TiO<sub>2</sub> heterostructured thin films.

The average crystallite size of c-SnO<sub>2</sub> thin film was estimated from the Equation (1) as 14 nm. Very weak and wide (101) and (211) diffraction peaks in XRD patterns of a-SnO<sub>2</sub> indicate that the crystallite size falls below 10 nm, thus the size effect in optical, electronic and sensory properties can be expected.

The morphology of TiO<sub>2</sub> synthesized by L–B method directly on silicon substrate and that of a-SnO<sub>2</sub> deposited by MS was investigated by SEM as shown in Figure 6. Figure 7 demonstrates SEM results for TiO<sub>2</sub> L–B layer on a-SnO<sub>2</sub> support. Top-view images reveal discontinuous layer composed of TiO<sub>2</sub> agglomerates (Figures 6a and 7c,d), which might result in an increased surface-to-volume ratio (Figure 7a), advantageous from the point of view of gas sensing. A similar morphology has been reported by Choudhary et al. [61] for ultrathin TiO<sub>2</sub> layers grown by the same technique.

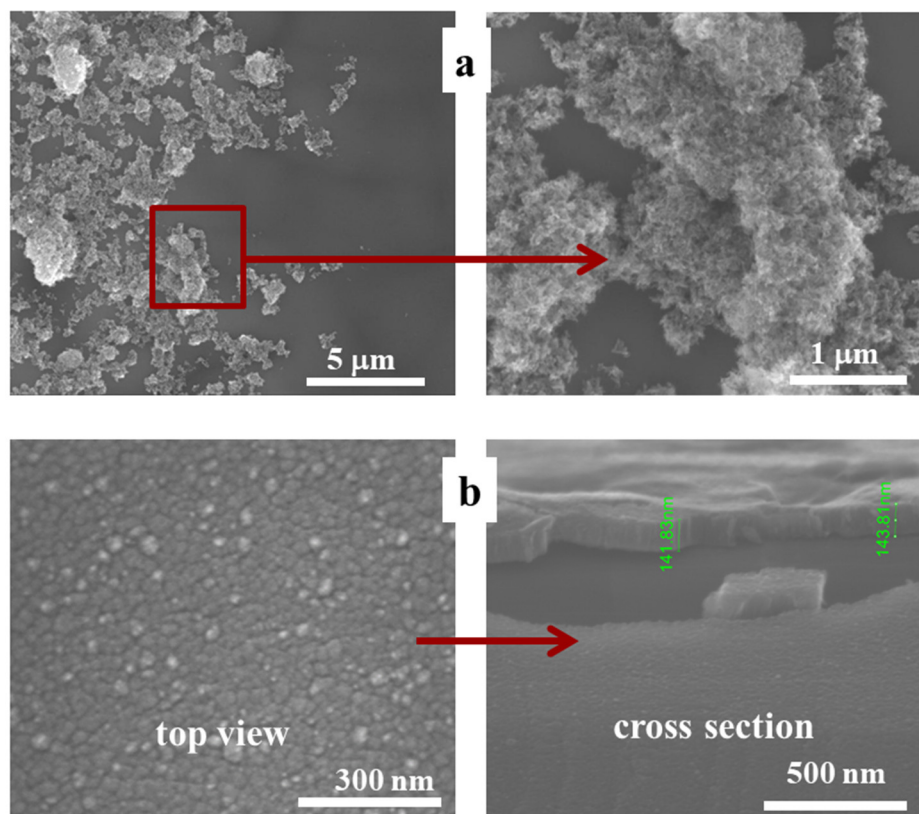


**Figure 6.** SEM images of thin films on Si substrate: (a)  $\text{TiO}_2$ , and (b)  $\text{a-SnO}_2$ .

As far as the morphology of  $\text{SnO}_2$  thin films deposited by sputtering is concerned, it is typical to observe a columnar mode of growth [37]. The cross-sectional images presented in Figures 6b and 7b reveal distinct columns of the diameter increasing in the direction towards the surface. The top view (Figure 6b) shows the relatively smooth surface of  $\text{a-SnO}_2$  with much bigger grains of  $\text{TiO}_2$  nanopowder deposited on top of  $\text{a-SnO}_2$  (Figure 7c,d). EDS mapping (Figure 7e,f) combined with the morphological image in Figure 7d confirms that the discontinuous form observed on the surface of  $\text{a-SnO}_2$  is composed of oxidized titanium.

Further proof of the stoichiometry of the layers deposited by the Langmuir–Blodgett technique has been given by X-ray photoelectron spectroscopy. The oxidation state of Ti ions at the surface of thin films obtained by the L–B method was established by XPS. The  $\text{Ti}2p$  and  $\text{O}1s$  spectra are presented in Figure 8a,b, respectively, and the Si peak coming from the substrate is shown in Figure 8c. Moreover, a doublet of  $\text{Sn } 3d_{5/2}$  and  $\text{Sn } 3d_{3/2}$  peaks from the  $\text{a-SnO}_2$  layer below can be seen in Figure 8d, supporting the SEM observation of discontinuous growth of  $\text{TiO}_2$ . The total area under the Si peak was used as a reference to calculate the relative area of Ti and O peaks. XPS spectra reveal two Ti peaks:  $\text{Ti}2p_{3/2}$  and  $\text{Ti}2p_{1/2}$  (at the position 458.7 eV and 464.4 eV, respectively) associated with spin-orbit splitting and assigned to  $\text{Ti}^{4+}$ . Binding energies BE: 487.3 eV and 495.7 eV corresponding to  $\text{Sn}3d_{5/2}$  and  $\text{Sn}3d_{3/2}$  XPS peaks, respectively, indicate the presence of  $\text{Sn}^{4+}$ . Recorded  $\text{O}1s$  XPS peaks are characteristic of the configuration: Ti–O and Si–O (coming from the substrate) with the binding energy 529.9 eV and 532.7 eV, respectively. The  $\text{O}1s$  peak at 534.0 eV peak can be attributed to –OH groups bounded to the surface of the sample. The O/Ti atomic ratio (calculated by taking into account the respective relative sensitivity factors [62] for the  $\text{Ti}2p_{3/2}$  peak and  $\text{O}1s$  peak) is equal to 2.63. The excess of oxygen indicates that the surface of  $\text{TiO}_2$  is over-oxidized as a consequence of adsorption of oxygen, which is important in the first step of gas sensing process.



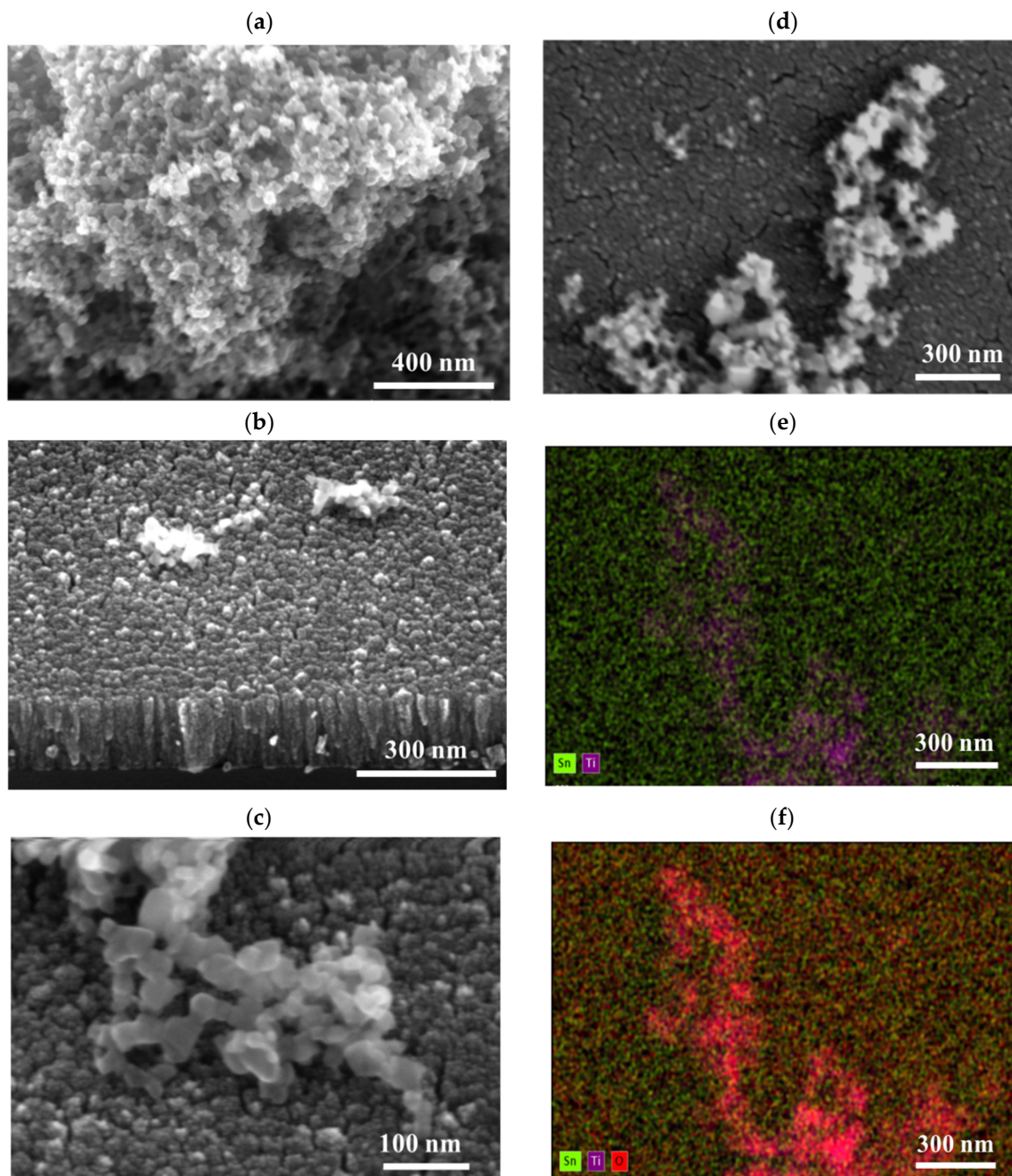


**Figure 7.** SEM images for  $\text{TiO}_2$  grown by the Langmuir–Blodgett method on the surface of a- $\text{SnO}_2$  thin films deposited by magnetron sputtering MS: cross sections (**a,b**), top view (**c,d**) and EDS maps of Sn, Ti, O elements (**e,f**).

Figure 9a,b present the transmittance and reflectance spectra of a- $\text{SnO}_2$  and c- $\text{SnO}_2$  thin films. The interference fringes of transmittance spectrum over low absorption region enabled us to determine the refractive index,  $n$ , using the envelope method proposed by Manificier et al. [63]. Knowing the wavelength positions of extrema in the transmittance spectrum and analysing the amplitude of transmittance coefficient, it is possible to find the film thickness. For a- $\text{SnO}_2$  sample, refractive index  $n = 1.73$  at wavelength  $\lambda = 700$  nm and the film thickness  $d = 190$  nm were found.

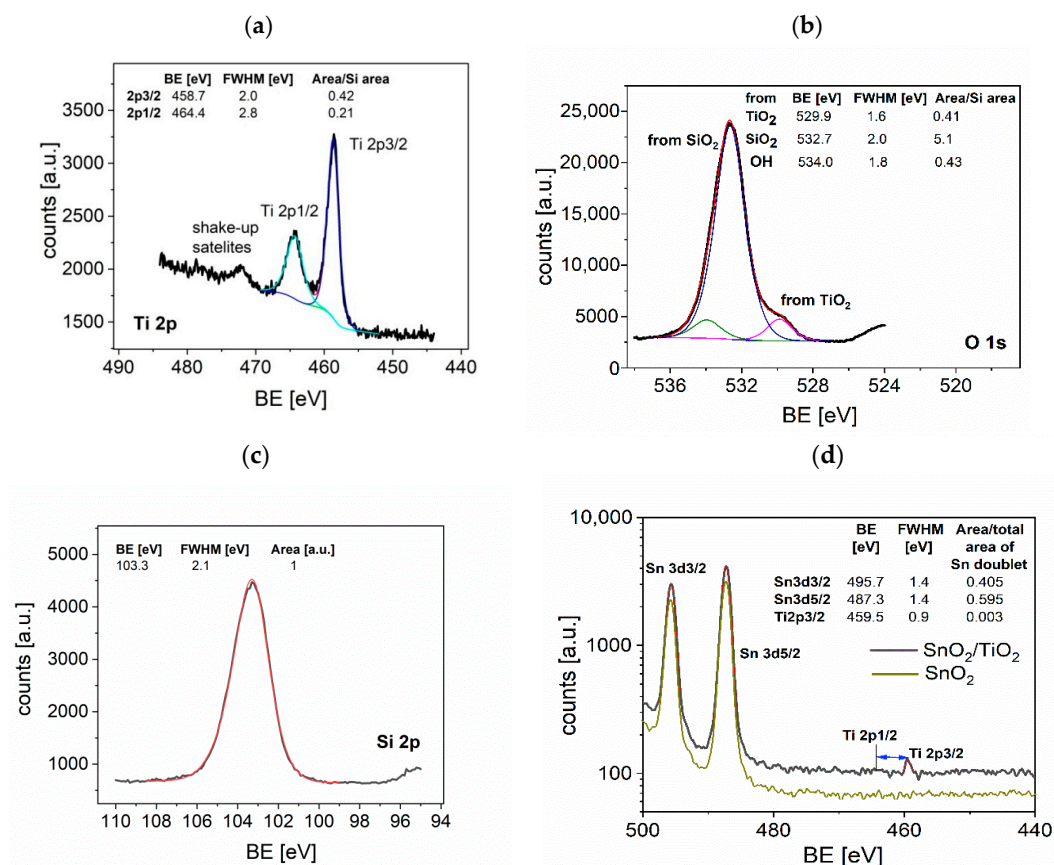


**Figure 8.** XPS spectra (a–c) of TiO<sub>2</sub> thin film deposited on Si substrate by the L–B technique: (a) Ti2p, (b) O1s, (c) Si2p, (d) TiO<sub>2</sub> thin film deposited on SnO<sub>2</sub> thin film by L–B technique; BE—binding energy.

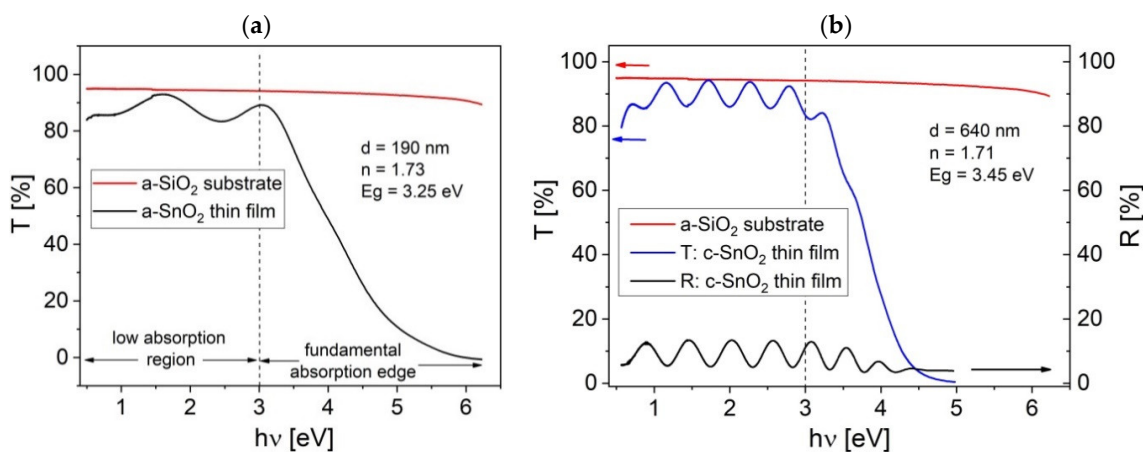


**Figure 9.** Spectral dependence of the transmittance, T, and reflectance, R, for (a) a-SnO<sub>2</sub>, (b) c-SnO<sub>2</sub> thin films; n—calculated refractive index, d—thickness derived from optical spectra; E<sub>g</sub>—band gap.

For c-SnO<sub>2</sub> film, the transmittance spectrum is richer in extrema because of an increased film thickness  $d = 640$  nm. Moreover, the extrema of the reflectance spectra extend over a wider spectral range than those corresponding to the transmittance. The refractive indices for a-SnO<sub>2</sub> and c-SnO<sub>2</sub> thin films are very close, which indicates a similar film density. However, both refractive indices are lower than those usually reported for SnO<sub>2</sub> ( $n > 2.0$ ) [64]. This may have been caused by the specific columnar growth observed in the SEM cross-sectional images (Figures 6b and 7b). The voids between the columns are probably filled with adsorbed oxygen and water molecules [64].

### 3.2. Gas Sensor Measurements

Gas sensor studies were carried out by following the procedure described in Section 2.2.

As one can see in Figure 10, both a-SnO<sub>2</sub> and SnO<sub>2</sub>/TiO<sub>2</sub> thin film sensors exhibit remarkable  $R_{NO_2}/R_0$  responses to 20 ppm NO<sub>2</sub> at 210 °C of about 500 and 1650, for pure a-SnO<sub>2</sub>, and SnO<sub>2</sub>/TiO<sub>2</sub> thin films, respectively. Deposition of TiO<sub>2</sub> onto SnO<sub>2</sub> improves not only the absolute value of the response but its kinetics as well. Moreover, SnO<sub>2</sub>/TiO<sub>2</sub> thin films reveal lower resistance in air  $R_0$ , probably due to the injection of electrons from TiO<sub>2</sub> to SnO<sub>2</sub>, which suggests formation of n-n heterojunction.

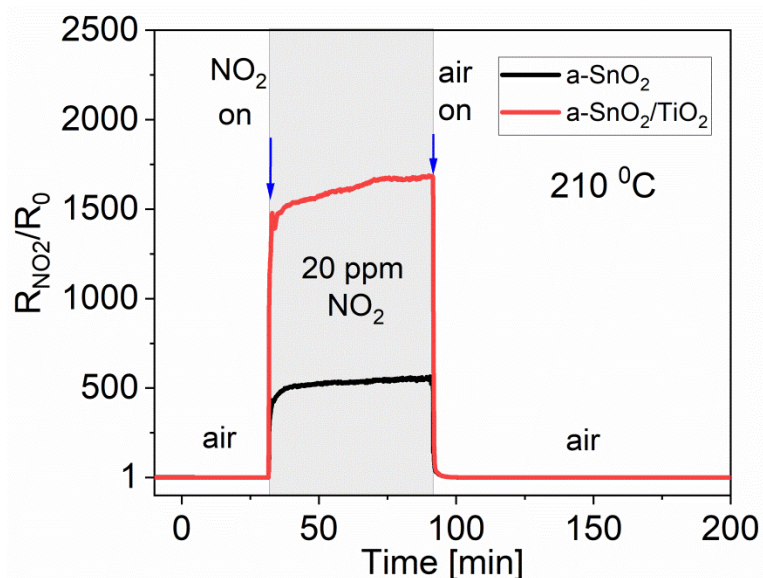


**Figure 10.** The gas sensor responses,  $R_{NO_2}/R_0$ , of a-SnO<sub>2</sub> and SnO<sub>2</sub>/TiO<sub>2</sub> upon exposure to 20 ppm NO<sub>2</sub> at 210 °C.

The response,  $R_{NO_2}/R_0$ , increases systematically when the working temperature decreases, as shown in Figure 11. This indicates a possible interference due to the physisorption of water molecules, which somehow helps in the detection of the oxidizing gas.

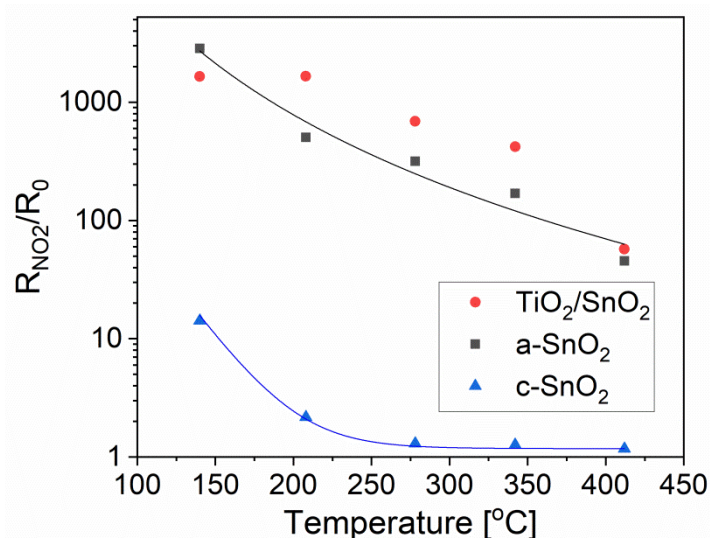


**Figure 11.** The  $R_{NO_2}/R_0$  responses to 20 ppm NO<sub>2</sub> of a-SnO<sub>2</sub>, c-SnO<sub>2</sub> and SnO<sub>2</sub>/TiO<sub>2</sub> thin films vs. operating temperature.



The same tendency is preserved for lower (400 ppb) concentration of  $\text{NO}_2$  in the case of  $\text{TiO}_2/\text{SnO}_2$  (Figure 12). At  $138^\circ\text{C}$ , the response of a- $\text{SnO}_2$  to 20 ppm  $\text{NO}_2$  reaches a very high value of about 3000 (Figure 11) while at  $123^\circ\text{C}$ , the response of  $\text{SnO}_2/\text{TiO}_2$  to 400 ppb  $\text{NO}_2$  is as high as 700 (Figure 12). The electrical resistance  $R_0$  in air decreases systematically with temperature, which is typical for semiconducting behaviour.

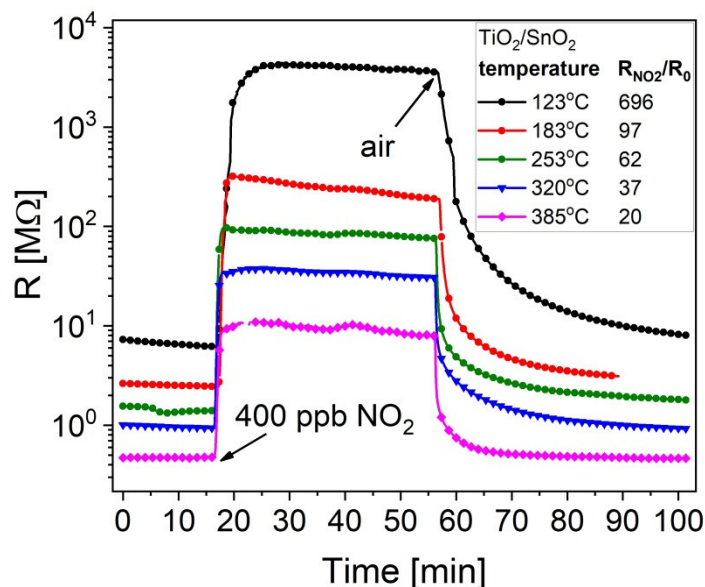


**Figure 12.** Dynamic changes in the electrical resistance of  $\text{SnO}_2/\text{TiO}_2$  thin films at different operating temperatures, upon exposure to 400 ppb  $\text{NO}_2$ .

Over the temperature range extending from 200 to  $350^\circ\text{C}$ ,  $\text{SnO}_2/\text{TiO}_2$  thin film exhibits a higher response than that of a- $\text{SnO}_2$ . As can be seen in Figure 11, within this temperature range, the response  $R_{\text{NO}_2}/R_0$  is 2.5 to 3 times higher for  $\text{SnO}_2/\text{TiO}_2$  compared with that of a- $\text{SnO}_2$ . It can be seen that amorphous  $\text{SnO}_2$  demonstrates much better sensing properties than crystalline  $\text{SnO}_2$ , probably due to the well known size effect [9] but at the same time, one cannot exclude the influence of film thickness on the gas response.

Figure 13 illustrates the responses of  $\text{SnO}_2/\text{TiO}_2$  thin films as a function of  $\text{NO}_2$  concentration down to 200 ppb at constant temperatures chosen within the range extending from  $120^\circ\text{C}$  to  $400^\circ\text{C}$ . Bi-layers of  $\text{SnO}_2/\text{TiO}_2$  are sensitive even to 200 ppb  $\text{NO}_2$  with the responses of  $390@123^\circ\text{C}$  and  $6.6@385^\circ\text{C}$ .

Based on the results discussed above, the analysis of kinetics of the response and the signal recovery was performed. As Table 2 shows, both response  $t_{\text{resp}}$  and recovery  $t_{\text{rec}}$  times gradually decrease with the increasing temperature and gas concentration. At all operating temperatures above  $150^\circ\text{C}$ ,  $t_{\text{resp}}$  is rather small and equals to about 4–12 s. The  $\text{SnO}_2/\text{TiO}_2$  sensor recovers relatively quickly,  $t_{\text{rec}}$  amounts to 9–28 s above  $150^\circ\text{C}$ . Such a fast reaction to  $\text{NO}_2$  and recovery in air are typical for low amounts of  $\text{NO}_2$  and suggest a dominant role of the surface adsorption processes due to the small film thickness.

Small values of  $t_{\text{resp}}$  and  $t_{\text{rec}}$  along with very good responses, observed at very low  $\text{NO}_2$  concentrations, make such a sensor very promising for environmental applications.

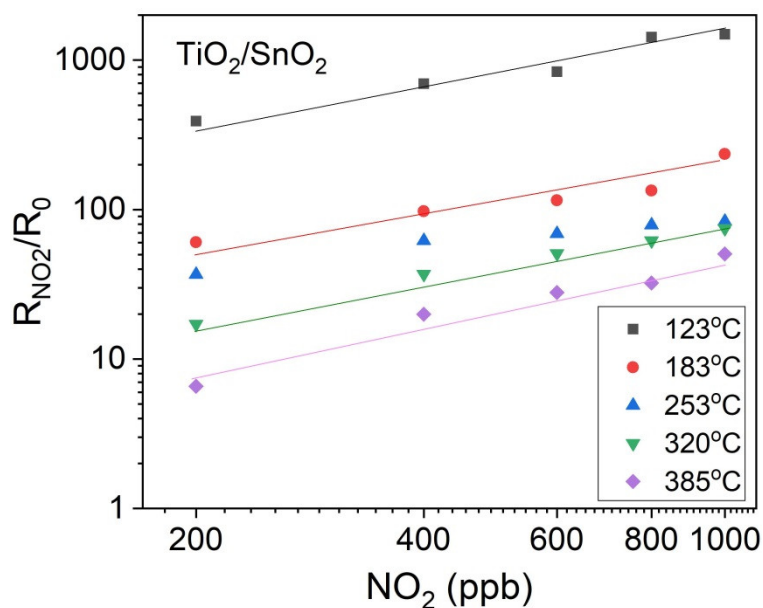


**Figure 13.** The SnO<sub>2</sub>/TiO<sub>2</sub> thin film response to low NO<sub>2</sub> concentrations at different operating temperatures.

**Table 2.** Kinetics of the SnO<sub>2</sub>/TiO<sub>2</sub> thin film response to NO<sub>2</sub> of two different concentrations;  $t_{\text{resp}}$ —response time,  $t_{\text{rec}}$ —recovery time.

Temperature [°C]	400 ppb NO <sub>2</sub>			2000 ppb NO <sub>2</sub>		
	$t_{\text{resp}}$ [s]	$t_{\text{rec}}$ [s]	$R_{\text{NO}_2}/R_0$	$t_{\text{resp}}$ [s]	$t_{\text{rec}}$ [s]	$R_{\text{NO}_2}/R_0$
123	62	42	696	26	58	847
183	11	22	97	10	9	350
253	10	17	62	4	10	136
320	12	28	37	4	11	101
385	12	19	20	4	-	-

The effects of interfering agents, such as a reducing gas and humidity, were taken into account, as demonstrated in Figures 14 and 15, respectively.

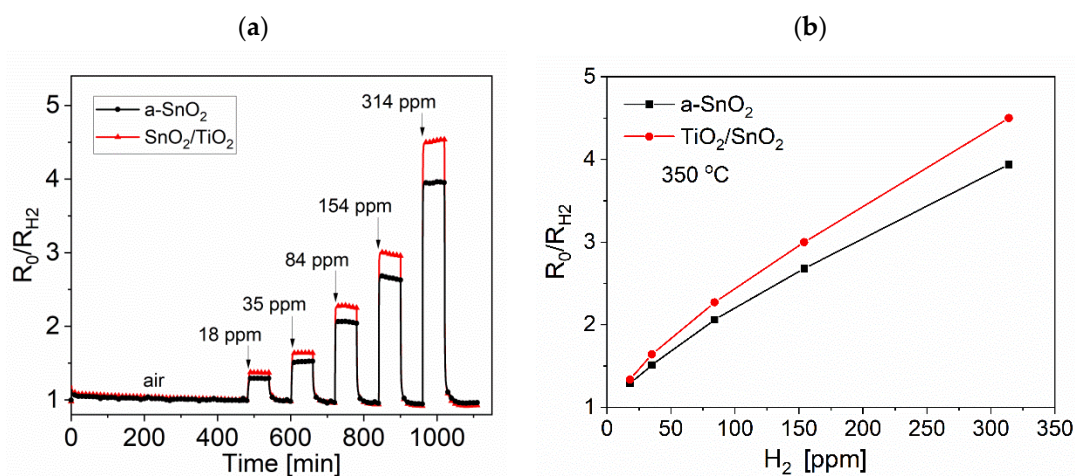


**Figure 14.** Responses  $R_0/R_{\text{H}_2}$  of a-SnO<sub>2</sub> and SnO<sub>2</sub>/TiO<sub>2</sub> thin films to step changes in H<sub>2</sub> measured according to scenario CT: (a) dynamic characteristics at 350 °C and (b) response as a function of H<sub>2</sub> concentration at 350 °C.



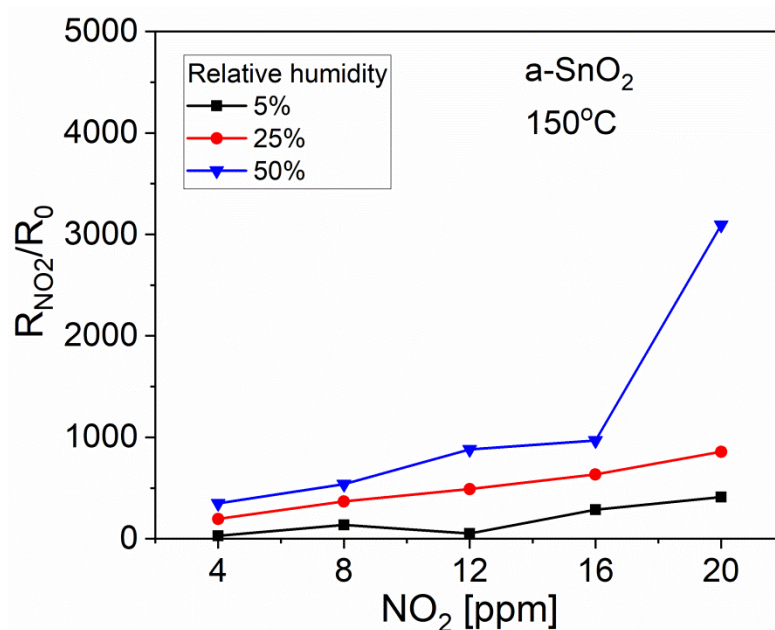


**Figure 15.** Influence of humidity on the  $R_{NO_2}/R_0$  responses of a-SnO<sub>2</sub> thin films to varying NO<sub>2</sub> concentrations at a constant operating temperature 150 °C.

The responses of both a-SnO<sub>2</sub> and SnO<sub>2</sub>/TiO<sub>2</sub> to the reducing gas H<sub>2</sub> are much smaller than those to NO<sub>2</sub>. The highest response to H<sub>2</sub> was observed at 350–400 °C, but even at 314 ppm the  $S_{H_2} = 3.9$  for a-SnO<sub>2</sub> layer and  $S_{H_2} = 4.5$  for SnO<sub>2</sub>/TiO<sub>2</sub> bi-layer. The decoration of SnO<sub>2</sub> with TiO<sub>2</sub> thin film improved the response to H<sub>2</sub> by only 18%.

As mentioned in Section 2.2, all the gas sensing measurements were performed at relative humidity RH = 50%. This level of humidity is treated as ‘normal’ because the sensors usually work under such environmental conditions. In order to investigate the influence of humidity on the sensing characteristics, a-SnO<sub>2</sub> sample was tested also at lower RH values, as shown in Figure 15 and Table 3. One can conclude that a higher humidity improves the response to NO<sub>2</sub>. The effect is the quite pronounced at lower operating temperature of 150 °C. The humidity interference is negligible at higher operating temperatures, which suggests a predominant role of the physisorption of molecular water over the chemisorption of OH<sup>−</sup> groups [16,65].

**Table 3.**  $R_{NO_2}/R_0$  responses of a-SnO<sub>2</sub> sensor to 12 ppm NO<sub>2</sub> at various temperatures and for different relative humidity values.

RH %	$R_{NO_2}/R_0$			
	150 °C	220 °C	235 °C	335 °C
5	51	-	-	13
25	489	135	127	-
50	881	147	128	-
75	-	94	60	-

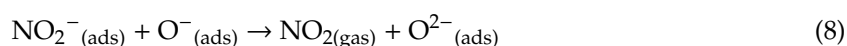
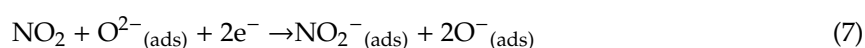
#### 4. Discussion

SnO<sub>2</sub> and TiO<sub>2</sub> are both n-type metal oxide semiconductors. Their sensing mechanism is controlled by the surface phenomena and their resistance changes upon exposure to different gas atmospheres. In the first step of gas sensing, it is usually assumed that oxygen is adsorbed in different atomic or

molecular forms, i.e.,  $O_2^-$ ,  $O^-$ , and  $O_2^-$  [66,67]. Such behaviour can be expressed by the following reactions (2–5):



The ionized oxygen  $O_2^-$  species dominate at temperatures below 150 °C [16], while for temperatures above 150 °C, the predominant oxygen forms are  $O^-$  and  $O^{2-}$ . When the sensor is exposed to pure air atmosphere at a constant temperature, the oxygen molecules adsorb at the sensing material surface, and capture free electrons from the conduction band. As a result, the sensor conductance decreases. After some time, an equilibrium is reached and the sensor resistance stabilizes. After exposure to  $NO_2$  oxidizing gas, the effect of electron capturing proceeds further (reaction 6). Moreover,  $NO_2^-$  ions can be created in reaction with previously adsorbed oxygen ions  $O_2^-(ads)$  (reaction 7). Reactions 6 and 7 cause a reduction of the sensor conductance. At the same time, a reverse reaction 8 with  $NO_2^-(ads)$  losing an electron may take place.



It should be stressed that reaction with  $NO_2$  can take place (reaction 6) without the presence of air (and therefore oxygen) because  $NO_2$  itself contains oxygen and forms an oxidizing agent. Reaction to  $NO_2$  in an oxygen-free atmosphere is therefore stronger than in an oxygen-rich one, because the oxygen molecules adsorbing at the surface reduce the number of free sites where  $NO_2$  adsorption can occur.

Tin dioxide,  $SnO_2$  has been successfully applied to  $NO_2$  detection, as can be concluded based on the publications listed in Table 1. Santos et al. [18] demonstrated the selective  $NO_2$  detection of low concentrations down to 100 ppb by thin films of  $SnO_2$  at 200 °C. The technology of  $SnO_2$  affects its morphology, which, as a consequence, influences the gas response and its kinetics. The examples of different methods of  $SnO_2$  synthesis—sol gel [19], chemical spray deposition [24], chemical vapor deposition [25] and vapor phase deposition [11]—were given. Modification of  $SnO_2$  by other metal oxides such as  $ZnO$ ,  $WO_3$ , and  $TiO_2$  was demonstrated as an efficient means to enhance the sensing performance. A very high response (as high as 12800) to 5 ppm  $NO_2$  at relatively low temperature of 150 °C was reported by Sukunta et al. [17] for heterostructures of  $SnO_2$  nanoparticles- $WO_3$  nanotubes. A specific morphology providing well developed surface is required for an improved gas sensing response. It is believed that the higher surface-to-volume ratio of the sensing material results in an increased density of active centers for chemisorption. Sharma et al. [23] published the results of extended studies on gas sensing with various structures:  $WO_3/SnO_2$ ,  $TeO_2/SnO_2$ ,  $CuO/SnO_2$ ,  $ZnO/SnO_2$  among which one can find  $TiO_2$  nano-thin micro-clusters loaded over  $SnO_2$  that manifested a relatively high response of 825 to 10 ppm  $NO_2$  at a low temperature of 90 °C.

The Langmuir–Blodgett technique is usually applied to form monolayers of amphiphilic molecules. Therefore, in attempts to use this method in gas-sensing applications, organic compounds such as porphyrin [68,69], benzenedicarboxylic acids [70], and polypyrrole [71] have been most frequently employed. Formation of  $TiO_2$  or  $SnO_2$  thin films is often associated with using precursors of metal oxides, e.g., titanium alkoxides [72], polyaniline- $TiO_2$  [73] or complexes of metal salts of fatty acid or amines, e.g., ODA-stannate complexes [74], or ODA- $KTiO_2$  [75]. Obtained films are then subject to a thermal decomposition which removes the organic part. Another method is to deposit organic amphiphilic particles with a chemical affinity to  $TiO_2$  or  $SnO_2$  derivatives. Then, the previously obtained layer is immersed in the proper solution (e.g., potassium titanium oxalate, PTO [76,77] or

SnO<sub>2</sub> derivatives) and thermally treated. There are few reports on using the L–B method to form thin films directly from crystallites of metal oxides [61,78,79].

Choudhary et al. [61] demonstrated the well developed surface morphology of TiO<sub>2</sub> layers grown using the Langmuir–Blodgett technique. The aggregation of nanoparticles and surface coverage can be tuned by the target surface pressure. It has been claimed [61] that discontinuous TiO<sub>2</sub> layers such as those observed in the course of our studies contain large amount of defects that favourably affect the sensor response. The same group from Bhabha Atomic Research Center, Mumbai, India published a series of papers [77,79] on SnO<sub>2</sub> and SnO<sub>2</sub>-TiO<sub>2</sub> thin films deposited by L–B method for gas sensing and photoelectrochemical application.

It is well known [65] that as the gas sensors usually operate in the atmosphere containing water, two processes can be responsible for H<sub>2</sub>O surface adsorption:

- physisorption of water in its molecular form that occurs at lower temperatures
- chemisorption of OH<sup>−</sup> taking place at higher temperatures above 300 °C

However, if both oxygen and water molecules are present in the atmosphere, there is a competitive adsorption between O<sub>2</sub><sup>−</sup> and H<sub>2</sub>O-related surface species. As a result, MOS responses to gases are distinctly different under dry and humidified atmospheres [80–82].

A decrease in the gas sensor response in the presence of elevated level of humidity is usually explained by a reduction of the effective sensing area. However, the opposite behaviour can also be seen when the detected molecule directly reacts with active hydroxyl groups OH, thus improving the sensor response [16]. In view of the results presented here, it can be assumed that the physisorption of water molecules is probably responsible for an increase in the NO<sub>2</sub> response as the most pronounced influence of humidity is observed at 150 °C. It is possible that at this relatively low temperature, there is a strong competition between oxygen and water adsorption. The elimination of the adsorption of oxygen species might be beneficial to NO<sub>2</sub> gas sensing, as already discussed (eq.6) the presence of oxygen is not necessary to form NO<sub>2</sub><sup>−</sup> sites at the sensor surface.

## 5. Conclusions

The SnO<sub>2</sub>/TiO<sub>2</sub> n-n thin film nanoheterostructures were obtained by depositing discontinuous TiO<sub>2</sub> thin films on previously sputtered thicker SnO<sub>2</sub> layers using the Langmuir–Blodgett technique with a nanopowder of rutile as a starting material. The morphological, structural and electronic properties of pure SnO<sub>2</sub> and SnO<sub>2</sub>/TiO<sub>2</sub> heterostructures and their responses to NO<sub>2</sub> gases were studied. The most important results of this research can be summarized as follows:

- The heterostructures composed of TiO<sub>2</sub> agglomerated discontinuous layer on the SnO<sub>2</sub> thin film with a columnar mode of growth have a higher gas response than pure SnO<sub>2</sub> for both reducing (H<sub>2</sub>) and oxidizing (NO<sub>2</sub>) gases.
- Amorphous a-SnO<sub>2</sub> demonstrate a much higher response to NO<sub>2</sub> than their crystalline counterparts c-SnO<sub>2</sub>, probably because of the size effect.
- SnO<sub>2</sub>/TiO<sub>2</sub> heterostructures are selective and sensitive even to low concentrations of NO<sub>2</sub> which can be attributed to the electron injection from the conduction band CB of TiO<sub>2</sub> to CB of SnO<sub>2</sub>.
- The significant increase in NO<sub>2</sub> response occurs at an operating temperature below 150 °C where a considerable influence of humidity has been demonstrated; this effect is probably due to the competitive physisorption of water against chemisorption of oxygen and hydroxyl groups.
- SnO<sub>2</sub>/TiO<sub>2</sub> n-n nanoheterostructures in a form of thin films have proven to be highly sensitive and selective to NO<sub>2</sub> with a threshold lower than 200 ppb.

**Author Contributions:** Conceptualization, K.Z., P.N., W.M.; methodology, W.M., A.R., K.K., M.Z., P.N.; validation, K.Z., W.M., A.R., K.K.; investigation, W.M., A.R., K.K., M.Z., P.N.; writing—original draft preparation, W.M., K.Z., P.N., K.K.; writing—review and editing, W.M., K.Z., P.N.; visualization, W.M.; supervision, K.Z., W.M.; project administration, P.N. All authors have read and agreed to the published version of the manuscript.

**Funding:** This research was funded by National Science Centre, Poland, grant number UMO-2016/23/B/ST7/00894 and the APC was funded by Ministry of Science and Higher Education, Poland, (program “Excellence initiative—research university” for the AGH University of Science and Technology).

**Conflicts of Interest:** The authors declare that they have no conflict of interest.

## References

1. U.S. National Library of Medicine, TOXNET—Toxicology Data Network, (n.d.). Available online: <https://toxnet.nlm.nih.gov> (accessed on 26 November 2018).
2. The National Institute for Occupational Safety and Health (NIOSH), Nitrogen Dioxide—International Chemical Safety Cards, (n.d.). Available online: <https://www.cdc.gov/niosh/ipcsneng/neng0930.html> (accessed on 26 November 2018).
3. Ielpo, P.; Mangia, C.; Marra, G.P.; Comite, V.; Rizza, U.; Uricchio, V.F.; Fermo, P. Outdoor spatial distribution and indoor levels of NO<sub>2</sub> and SO<sub>2</sub> in a high environmental risk site of the South Italy. *Sci. Total Environ.* **2019**, *648*, 787–797. [[CrossRef](#)] [[PubMed](#)]
4. Casquero-Vera, J.A.; Lyamani, H.; Titos, G.; Borrás, E.; Olmo, F.J.; Alados-Arboledas, L. Impact of primary NO<sub>2</sub> emissions at different urban sites exceeding the European NO<sub>2</sub> standard limit. *Sci. Total Environ.* **2019**, *646*, 1117–1125. [[CrossRef](#)] [[PubMed](#)]
5. Salthammer, T.; Schieweck, A.; Gu, J.; Ameri, S.; Uhde, E. Future trends in ambient air pollution and climate in Germany—Implications for the indoor environment. *Build. Environ.* **2018**, *143*, 661–670. [[CrossRef](#)]
6. Mölter, A.; Lindley, S.; de Vocht, F.; Agius, R.; Kerry, G.; Johnson, K.; Ashmore, M.; Terry, A.; Dimitroulopoulou, S.; Simpson, A. Performance of a microenvironmental model for estimating personal NO<sub>2</sub> exposure in children. *Atmos. Environ.* **2012**, *51*, 225–233. [[CrossRef](#)]
7. Beulertz, G.; Groß, A.; Moos, R.; Kubinski, D.J.; Visser, J.H. Determining the total amount of NO<sub>x</sub> in a gas stream—Advances in the accumulating gas sensor principle. *Sens. Actuators B* **2012**, *175*, 157–162. [[CrossRef](#)]
8. Keskinen, H.; Tricoli, A.; Marjamäki, M.; Mäkelä, J.M.; Pratsinis, S.E. Size-selected agglomerates of SnO<sub>2</sub> nanoparticles as gas sensors. *J. Appl. Phys.* **2009**, *106*, 084316. [[CrossRef](#)]
9. Xu, C.; Tamaki, J.; Miura, N.; Yamazoe, N. Grain size effects on gas sensitivity of porous SnO<sub>2</sub>-based elements. *Sens. Actuators B* **1991**, *3*, 147–155. [[CrossRef](#)]
10. Korotcenkov, G.; Brinzari, V.; Han, S.H.; Gulina, L.B.; Tolstoy, V.P.; Cho, B.K. SnO<sub>2</sub> films decorated by Au clusters and their gas sensing properties. *Mater. Sci. Forum* **2015**, *827*, 251–256. [[CrossRef](#)]
11. Comini, E.; Faglia, G.; Sberveglieri, G.; Calestani, D.; Zanotti, L.; Zha, M. Tin oxide nanobelts electrical and sensing properties. *Sens. Actuators B* **2005**, *111–112*, 2–6. [[CrossRef](#)]
12. Shukla, S.; Patil, S.; Kuiry, S.C.; Rahman, Z.; Du, T.; Ludwig, L.; Parish, C.; Seal, S. Synthesis and characterization of sol–gel derived nanocrystalline tin oxide thin film as hydrogen sensor. *Sens. Actuators B* **2003**, *96*, 343–353. [[CrossRef](#)]
13. Alberti, A.; Renna, L.; Sanzaro, S.; Smecca, E.; Mannino, G.; Bongiorno, C.; Galati, C.; Gervasi, L.; Santangelo, A.; La Magna, A. Innovative spongy TiO<sub>2</sub> layers for gas detection at low working temperature. *Sens. Actuators B* **2018**, *259*, 658–667. [[CrossRef](#)]
14. Huang, L.; Liu, T.; Zhang, H.; Guo, W.; Zeng, W. Hydrothermal synthesis of different TiO<sub>2</sub> nanostructures: Structure, growth and gas sensor properties. *J. Mater. Sci. Mater. Electron.* **2012**, *23*, 2024–2029. [[CrossRef](#)]
15. Wang, C.; Yin, L.; Zhang, L.; Qi, Y.; Lun, N.; Liu, N. Large scale synthesis and gas-sensing properties of anatase TiO<sub>2</sub> three-dimensional hierarchical nanostructures. *Langmuir* **2010**, *26*, 12841–12848. [[CrossRef](#)] [[PubMed](#)]
16. Haidry, A.A.; Kind, N.; Saruhan, B. Investigating the influence of Al-doping and background humidity on NO<sub>2</sub> sensing characteristics of magnetron-sputtered SnO<sub>2</sub> sensors. *J. Sens. Sens. Syst.* **2015**, *4*, 271–280. [[CrossRef](#)]
17. Sukunta, J.; Wisitorsaat, A.; Tuantranont, A.; Phanichphant, S.; Liewhiran, C. WO<sub>3</sub> nanotubes–SnO<sub>2</sub> nanoparticles heterointerfaces for ultrasensitive and selective NO<sub>2</sub> detections. *Appl. Surf. Sci.* **2018**, *458*, 319–332. [[CrossRef](#)]
18. Santos, J.; Serrini, P.; O’Beirn, B.; Manes, L. A thin film SnO<sub>2</sub> gas sensor selective to ultra-low NO<sub>2</sub> concentrations in air. *Sens. Actuators B* **1997**, *43*, 154–160. [[CrossRef](#)]

19. Kaur, J.; Kumar, R.; Bhatnagar, M.C. Effect of indium-doped SnO<sub>2</sub> nanoparticles on NO<sub>2</sub> gas sensing properties. *Sens. Actuators B* **2007**, *126*, 478–484. [[CrossRef](#)]
20. Liangyuan, C.; Shouli, B.; Guojun, Z.; Dianqing, L.; Aifan, C.; Liu, C.C. Synthesis of ZnO–SnO<sub>2</sub> nanocomposites by microemulsion and sensing properties for NO<sub>2</sub>. *Sens. Actuators B* **2008**, *134*, 360–366. [[CrossRef](#)]
21. Bai, S.; Li, D.; Han, D.; Luo, R.; Chen, A.; Chung, C.L. Preparation, characterization of WO<sub>3</sub>–SnO<sub>2</sub> nanocomposites and their sensing properties for NO<sub>2</sub>. *Sens. Actuators B* **2010**, *150*, 749–755. [[CrossRef](#)]
22. Chen, A.; Huang, X.; Tong, Z.; Bai, S.; Luo, R.; Liu, C.C. Preparation, characterization and gas-sensing properties of SnO<sub>2</sub>–In<sub>2</sub>O<sub>3</sub> nanocomposite oxides. *Sens. Actuators B* **2006**, *115*, 316–321. [[CrossRef](#)]
23. Sharma, A.; Tomar, M.; Gupta, V. Enhanced response characteristics of SnO<sub>2</sub> thin film based NO<sub>2</sub> gas sensor integrated with nanoscaled metal oxide clusters. *Sens. Actuators B* **2013**, *181*, 735–742. [[CrossRef](#)]
24. Leo, G.; Rella, R.; Siciliano, P.; Capone, S.; Alonso, J.C.; Pankov, V.; Ortiz, A. Sprayed SnO<sub>2</sub> thin films for NO<sub>2</sub> sensors. *Sens. Actuators B* **1999**, *58*, 370–374. [[CrossRef](#)]
25. Sauvan, M.; Pijolat, C. Selectivity improvement of SnO<sub>2</sub> films by superficial metallic films. *Sens. Actuators B* **1999**, *58*, 295–301. [[CrossRef](#)]
26. Bang, J.H.; Choi, M.S.; Mirzaei, A.; Kwon, Y.J.; Kim, S.S.; Kim, T.W.; Kim, H.W. Selective NO<sub>2</sub> sensor based on Bi<sub>2</sub>O<sub>3</sub> branched SnO<sub>2</sub> nanowires. *Sens. Actuators B* **2018**, *274*, 356–369. [[CrossRef](#)]
27. Srivastava, V.; Jain, K. At room temperature graphene/SnO<sub>2</sub> is better than MWCNT/SnO<sub>2</sub> as NO<sub>2</sub> gas sensor. *Mater. Lett.* **2016**, *169*, 28–32. [[CrossRef](#)]
28. Wang, Y.; Liu, C.; Wang, Z.; Song, Z.; Zhou, X.; Han, N.; Chen, Y. Sputtered SnO<sub>2</sub>:NiO thin films on self-assembled Au nanoparticle arrays for MEMS compatible NO<sub>2</sub> gas sensors. *Sens. Actuators B* **2019**, *278*, 28–38. [[CrossRef](#)]
29. Kamble, D.L.; Harale, N.S.; Patil, V.L.; Patil, P.S.; Kadam, L.D. Characterization and NO<sub>2</sub> gas sensing properties of spray pyrolyzed SnO<sub>2</sub> thin films. *J. Anal. Appl. Pyrolysis* **2017**, *127*, 38–46. [[CrossRef](#)]
30. Gu, D.; Li, X.; Zhao, Y.; Wang, J. Enhanced NO<sub>2</sub> sensing of SnO<sub>2</sub>/SnS<sub>2</sub> heterojunction based sensor. *Sens. Actuators B* **2017**, *244*, 67–76. [[CrossRef](#)]
31. Hyodo, T.; Urata, K.; Kamada, K.; Ueda, T.; Shimizu, Y. Semiconductor-type SnO<sub>2</sub>-based NO<sub>2</sub> sensors operated at room temperature under UV-light irradiation. *Sens. Actuators B* **2017**, *253*, 630–640. [[CrossRef](#)]
32. Yu, H.; Yang, T.; Wang, Z.; Li, Z.; Zhao, Q.; Zhang, M. p-N heterostructural sensor with SnO–SnO<sub>2</sub> for fast NO<sub>2</sub> sensing response properties at room temperature. *Sens. Actuators B Chem.* **2018**, *258*, 517–526. [[CrossRef](#)]
33. Wang, Z.; Jia, Z.; Li, Q.; Zhang, X.; Sun, W.; Sun, J.; Liu, B.; Ha, B. The enhanced NO<sub>2</sub> sensing properties of SnO<sub>2</sub> nanoparticles/reduced graphene oxide composite. *J. Colloid Interface Sci.* **2019**, *537*, 228–237. [[CrossRef](#)]
34. Li, Z.; Yi, J. Synthesis and enhanced NO<sub>2</sub>-sensing properties of ZnO-decorated SnO<sub>2</sub> microspheres. *Mater. Lett.* **2019**, *236*, 570–573. [[CrossRef](#)]
35. Liu, D.; Tang, Z.; Zhang, Z. Visible light assisted room-temperature NO<sub>2</sub> gas sensor based on hollow SnO<sub>2</sub>@SnS<sub>2</sub> nanostructures. *Sens. Actuators B* **2020**, *324*, 128754. [[CrossRef](#)]
36. Sharma, B.; Sharma, A.; Joshi, M.; Myung, J. Sputtered SnO<sub>2</sub>/ZnO heterostructures for improved NO<sub>2</sub> gas sensing properties. *Chemosensors* **2020**, *8*, 67. [[CrossRef](#)]
37. Maziarz, W. TiO<sub>2</sub>/SnO<sub>2</sub> and TiO<sub>2</sub>/CuO thin film nanoheterostructures as gas sensors. *Appl. Surf. Sci.* **2019**, *480*, 361–370. [[CrossRef](#)]
38. Kusior, A.; Radecka, M.; Zych, Ł.; Zakrzewska, K.; Reszka, A.; Kowalski, B.J. Sensitization of TiO<sub>2</sub>/SnO<sub>2</sub> nanocomposites for gas detection. *Sens. Actuators B* **2013**, *189*, 251–259. [[CrossRef](#)]
39. Zeng, W.; Liu, T.; Wang, Z. Sensitivity improvement of TiO<sub>2</sub>-doped SnO<sub>2</sub> to volatile organic compounds. *Phys. E Low-Dimens. Syst. Nanostruct.* **2010**, *43*, 633–638. [[CrossRef](#)]
40. Park, S.; Kim, S.; Kheel, H.; Park, S.E.; Lee, C. Synthesis and hydrogen gas sensing properties of TiO<sub>2</sub>-decorated CuO nanorods. *Bull. Korean Chem. Soc.* **2015**, *36*, 2458–2463. [[CrossRef](#)]
41. Shao, F.; Hoffmann, M.W.G.; Prades, J.D.; Zamani, R.; Arbiol, J.; Morante, J.R.; Varechkina, E.; Rumyantseva, M.; Gaskov, A.; Giebelhaus, I.; et al. Heterostructured p-CuO (nanoparticle)/n-SnO<sub>2</sub> (nanowire) devices for selective H<sub>2</sub>S detection. *Sens. Actuators B* **2013**, *181*, 130–135. [[CrossRef](#)]
42. Kaur, M.; Dadhich, B.K.; Singh, R.; Kailasaganapathi, S.; Bagwaiya, T.; Bhattacharya, S.; Debnath, A.K.; Muthe, K.P.; Gadkari, S.C. RF sputtered SnO<sub>2</sub>: NiO thin films as sub-ppm H<sub>2</sub>S sensor operable at room temperature. *Sens. Actuators B* **2017**, *242*, 389–403. [[CrossRef](#)]



43. Poloju, M.; Jayababu, N.; Ramana Reddy, M.V. Improved gas sensing performance of Al doped ZnO/CuO nanocomposite based ammonia gas sensor. *Mater. Sci. Eng. B Solid-State Mater. Adv. Technol.* **2018**, *227*, 61–67. [[CrossRef](#)]
44. Larin, A.; Womble, P.C.; Dobrokhotov, V. Hybrid SnO<sub>2</sub>/TiO<sub>2</sub> nanocomposites for selective detection of ultra-low hydrogen sulfide concentrations in complex backgrounds. *Sensors* **2016**, *16*, 1373. [[CrossRef](#)] [[PubMed](#)]
45. Miller, D.R.; Akbar, S.A.; Morris, P.A. Nanoscale metal oxide-based heterojunctions for gas sensing: A review. *Sens. Actuators B Chem.* **2014**, *204*, 250–272. [[CrossRef](#)]
46. Lyson-Sypien, B.; Kusior, A.; Rekas, M.; Zukrowski, J.; Gajewska, M.; Michalow-Mauke, K.; Graule, T.; Radecka, M.; Zakrzewska, K. Nanocrystalline TiO<sub>2</sub>/SnO<sub>2</sub> heterostructures for gas sensing. *Beilstein J. Nanotechnol.* **2017**, *8*, 108–122. [[CrossRef](#)] [[PubMed](#)]
47. Zakrzewska, K.; Radecka, M. TiO<sub>2</sub>-SnO<sub>2</sub> system for gas sensing-photodegradation of organic contaminants. *Thin Solid Films* **2007**, *515*, 8332–8338. [[CrossRef](#)]
48. Zakrzewska, K.; Radecka, M. TiO<sub>2</sub>-based nanomaterials for gas sensing—influence of anatase and rutile contributions. *Nanoscale Res. Lett.* **2017**, *12*, 89. [[CrossRef](#)]
49. McNamee, C.E.; Yamamoto, S.; Butt, H.J.; Higashitani, K. A straightforward way to form close-packed TiO<sub>2</sub> particle monolayers at an air/water interface. *Langmuir* **2011**, *27*, 887–894. [[CrossRef](#)]
50. Ganguly, P.; Paranjape, D.V.; Sastry, M. Novel structure of Langmuir-Blodgett films of chloroplatinic acid using n-octadecylamine: Evidence for interdigitation of hydrocarbon chains. *J. Am. Chem. Soc.* **1993**, *115*, 793–794. [[CrossRef](#)]
51. Choudhury, S.; Bagkar, N.; Dey, G.K.; Subramanian, H.; Yakhmi, J.V. Crystallization of prussian blue analogues at the air-water interface using an octadecylamine monolayer as a template. *Langmuir* **2002**, *18*, 7409–7414. [[CrossRef](#)]
52. Amm, D.T.; Johnson, D.J.; Laursen, T.; Gupta, S.K. Fabrication of ultrathin metal oxide films using Langmuir-Blodgett deposition. *Appl. Phys. Lett.* **1992**, *61*, 522–524. [[CrossRef](#)]
53. Paranjape, D.V.; Sastry, M.; Ganguly, P. Deposition of thin films of TiO<sub>2</sub> from Langmuir-Blodgett film precursors. *Appl. Phys. Lett.* **1993**, *63*, 18–20. [[CrossRef](#)]
54. Schurr, M.; Hassmann, J.; Kügler, R.; Tomaschko, C.; Voit, H. Ultrathin layers of rare earth oxides from Langmuir-Blodgett films. *Thin Solid Films* **1997**, *307*, 260–265. [[CrossRef](#)]
55. Kwon, H.; Yoon, J.S.; Lee, Y.; Kim, D.Y.; Baek, C.K.; Kim, J.K. An array of metal oxides nanoscale hetero p-n junctions toward designable and highly-selective gas sensors. *Sens. Actuators B Chem.* **2018**, *255*, 1663–1670. [[CrossRef](#)]
56. Nowak, P.; Maziarz, W.; Rydosz, A.; Kowalski, K.; Zakrzewska, K. SnO<sub>2</sub>/TiO<sub>2</sub> thin film n-n heterostructures for H<sub>2</sub> and NO<sub>2</sub> gas sensor. In Proceedings of the 17th International Meeting on Chemical Sensors—IMCS 2018, Vienna, Austria, 15–19 July 2018; pp. 549–550. [[CrossRef](#)]
57. Zakrzewska, K.; Maziarz, W.; Schneider, K.; Mazur, M.; Wojcieszak, D.; Kaczmarek, D. Cu<sub>2</sub>O/CuO thin film p-p nano-heterostructures for gas sensing. In Proceedings of the 17th International Meeting on Chemical Sensors—IMCS 2018, Vienna, Austria, 15–19 July 2018; pp. 789–790. [[CrossRef](#)]
58. Rydosz, A.; Maziarz, W.; Brudnik, A.; Czapla, A.; Zakrzewska, K. CuO and CuO/TiO<sub>2-y</sub> thin-film gas sensors of H<sub>2</sub> and NO<sub>2</sub>. In Proceedings of the XV International Scientific Conference on Optoelectronic and Electronic Sensors (COE), Warsaw, Poland, 17–20 June 2018; pp. 2016–2019.
59. Xu, H.; Ju, J.; Li, W.; Zhang, J.; Wang, J.; Cao, B. Superior triethylamine-sensing properties based on TiO<sub>2</sub>/SnO<sub>2</sub> n-n heterojunction nanosheets directly grown on ceramic tubes. *Sens. Actuators B* **2016**, *228*, 634–642. [[CrossRef](#)]
60. Maziarz, W.; Kusior, A.; Trenczek-Zajac, A. Nanostructured TiO<sub>2</sub>-based gas sensors with enhanced sensitivity to reducing gases. *Beilstein J. Nanotechnol.* **2016**, *7*, 1718–1726. [[CrossRef](#)]
61. Choudhary, K.; Manjuladevi, V.; Gupta, R.K.; Bhattacharyya, P.; Hazra, A.; Kumar, S. Ultrathin films of TiO<sub>2</sub> nanoparticles at interfaces. *Langmuir* **2015**, *31*, 1385–1392. [[CrossRef](#)]
62. Briggs, D.; Seah, M.P. (Eds.) *Practical Surface Analysis*, 2nd ed.; Wiley: Chichester, UK; New York, NY, USA, 1990.
63. Manifacier, J.C.; Gasiot, J.; Fillard, J.P. A simple method for the determination of the optical constants n, k and the thickness of a weakly absorbing thin film. *J. Phys. E* **1976**, *9*, 1002. [[CrossRef](#)]

64. Goldsmith, S.; Çetinörgü, E.; Boxman, R.L. Modeling the optical properties of tin oxide thin films. *Thin Solid Films* **2009**, *517*, 5146–5150. [[CrossRef](#)]
65. Barsan, N.; Weimar, U. Understanding the fundamental principles of metal oxide based gas sensors; The example of CO sensing with SnO<sub>2</sub> sensors in the presence of humidity. *J. Phys. Condens. Matter*. **2003**, *15*, R813–R839. [[CrossRef](#)]
66. Barsan, N.; Weimar, U. Conduction model of metal oxide gas sensors. *J. Electroceram.* **2001**, *7*, 143–167. [[CrossRef](#)]
67. Bielański, A.; Haber, J. Oxygen in catalysis on transition metal oxides. *Catal. Rev.* **1979**, *19*, 1–41. [[CrossRef](#)]
68. Giancane, G.; Valli, L. State of art in porphyrin Langmuir-Blodgett films as chemical sensors. *Adv. Colloid Interface Sci.* **2012**, *171–172*, 17–35. [[CrossRef](#)] [[PubMed](#)]
69. Capan, İ.; Tarımcı, Ç.; Capan, R. Fabrication of Langmuir–Blodgett thin films of porphyrins and investigation on their gas sensing properties. *Sens. Actuators B* **2010**, *144*, 126–130. [[CrossRef](#)]
70. Balcerzak, A.; Aleksiejuk, M.; Zhavnerko, G.; Agabekov, V. Sensing properties of two-component Langmuir-Blodgett layer and its porous derivative in SAW sensor for vapors of methanol and ethanol. *Thin Solid Films* **2010**, *518*, 3402–3406. [[CrossRef](#)]
71. Penza, M.; Milella, E.; Musio, F.; Alba, M.B.; Cassano, G.; Quirini, A. AC and DC measurements on Langmuir-Blodgett polypyrrole films for selective NH<sub>3</sub> gas detection. *Mater. Sci. Eng. C.* **1998**, *5*, 255–258. [[CrossRef](#)]
72. Oswald, M.; Hessel, V.; Riedel, R. Formation of ultra-thin ceramic TiO<sub>2</sub> films by the Langmuir-Blodgett technique—A two-dimensional sol-gel process at the air-water interface. *Thin Solid Films* **1999**, *339*, 284–289. [[CrossRef](#)]
73. Bhullar, G.K.; Kaur, R.; Raina, K.K. Hybrid polyaniline-TiO<sub>2</sub> nanocomposite Langmuir-Blodgett thin films: Self-assembly and their characterization. *J. Appl. Polym. Sci.* **2015**, *132*. [[CrossRef](#)]
74. Choudhury, S.; Betty, C.A.; Girija, K.G.; Kulshreshtha, S.K. Room temperature gas sensitivity of ultrathin SnO<sub>2</sub> films prepared from Langmuir-Blodgett film precursors. *Appl. Phys. Lett.* **2006**, *89*, 071914. [[CrossRef](#)]
75. Ganguly, P.; Paranjape, D.V.; Sastry, M. Studies on the deposition of titanyl oxalate ions using long-chain hydrocarbon amines. *Langmuir* **1993**, *9*, 577–579. [[CrossRef](#)]
76. Takahashi, M.; Kobayashi, K.; Tajima, K. Structural characterization and photocatalytic activity of ultrathin TiO<sub>2</sub> films fabricated by Langmuir–Blodgett technique with octadecylamine. *Thin Solid Films* **2011**, *519*, 8077–8084. [[CrossRef](#)]
77. Choudhury, S.; Betty, C.A. A heterostructured SnO<sub>2</sub>–TiO<sub>2</sub> thin film prepared by Langmuir–Blodgett technique. *Mater. Chem. Phys.* **2013**, *141*, 440–444. [[CrossRef](#)]
78. Betty, C.A.; Choudhury, S.; Girija, K.G. Discerning specific gas sensing at room temperature by ultrathin SnO<sub>2</sub> films using impedance approach. *Sens. Actuators B* **2012**, *173*, 781–788. [[CrossRef](#)]
79. Betty, C.A.; Choudhury, S.; Girija, K.G. Reliability studies of highly sensitive and specific multi-gas sensor based on nanocrystalline SnO<sub>2</sub> film. *Sens. Actuators B* **2014**, *193*, 484–491. [[CrossRef](#)]
80. Sahm, T.; Gurlo, A.; Bârsan, N.; Weimar, U.; Mädler, L. Fundamental studies on SnO<sub>2</sub> by means of simultaneous work function change and conduction measurements. *Thin Solid Films* **2005**, *490*, 43–47. [[CrossRef](#)]
81. Hahn, S.; Bârsan, N.; Weimar, U.; Ejakov, S.; Visser, J.; Soltis, R. CO sensing with SnO<sub>2</sub> thick film sensors: Role of oxygen and water vapour. *Thin Solid Films* **2003**, *436*, 17–24. [[CrossRef](#)]
82. Korotcenkov, G.; Blinov, I.; Brinzari, V.; Stetter, J.R. Effect of air humidity on gas response of SnO<sub>2</sub> thin film ozone sensors. *Sens. Actuators B* **2007**, *122*, 519–526. [[CrossRef](#)]

**Publisher’s Note:** MDPI stays neutral with regard to jurisdictional claims in published maps and institutional affiliations.



© 2020 by the authors. Licensee MDPI, Basel, Switzerland. This article is an open access article distributed under the terms and conditions of the Creative Commons Attribution (CC BY) license (<http://creativecommons.org/licenses/by/4.0/>).